Article:
Farr, N.T.H., Briceno de Gutierrez, M., S'ari, M. et al. (2026) Secondary electron hyperspectral imaging (SEHI) in FIB – SEM for proton exchange membrane fuel cells technology. ACS Omega. ISSN: 2470-1343

https://doi.org/10.1021/acsomega.5c09325

ACS OMEGA

Open Access

http://pubs.acs.org/journal/acsodf

Article

Secondary Electron Hyperspectral Imaging (SEHI) in FIB – SEM for Proton Exchange Membrane Fuel Cells Technology

Nicholas T. H. Farr,* Martha Briceno de Gutierrez, Mark S'ari, Ben Garton, Jingqiong Zhang, Lyudmila S. Mihaylova, and Cornelia Rodenburg

Cite This: https://doi.org/10.1021/acsomega.5c09325

Read Online

ACCESS | Metrics & More | Article Recommendations | Supporting Information

ABSTRACT: The performance of proton exchange membrane (PEM) fuel cells critically depends on the microstructure and chemistry of their constituent materials, particularly the catalyst layer (CL), carbon black (CB), ionomer films, and reinforced membranes. However, the highly heterogeneous and nanoscale nature of these components presents significant challenges for existing characterization techniques. This study explores the application of Secondary Electron Hyperspectral Imaging (SEHI) in focused ion beam−scanning electron microscopy (FIB−SEM) to address these limitations. SEHI uniquely integrates chemical sensitivity, surface specificity, and nanoscale spatial resolution, enabling detailed insights into key functional materials. Carbon black analysis revealed the spatial distribution of graphitised regions and surface functional groups, such as CO bonding, which are critical for optimizing electron transport and catalyst stability. For ionomer films and membranes, SEHI identified and mapped chemical differences between the ionomer matrix and its polybenzimidazole (PBI) reinforcement, distinguishing nitrogen species and surface functionalities. This capability facilitates a deeper understanding of how membrane composition and structure influence conductivity and durability. The results demonstrate SEHI's potential as a transformative tool for the nanoscale characterization of PEM fuel cell components, providing critical insights for the design and optimization of high-performance, durable fuel cells.

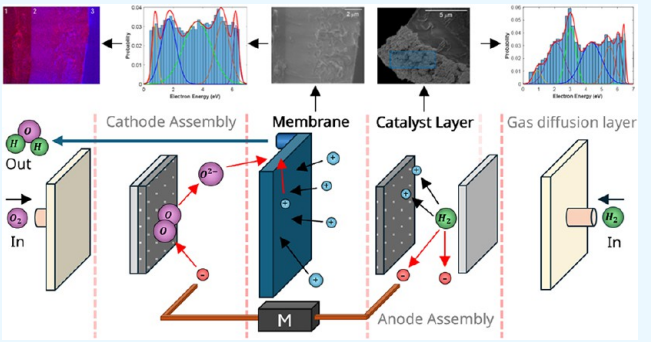

1. INTRODUCTION

Proton exchange membrane fuel cells (PEMFCs) are a vital technology in the transition to sustainable energy, offering high efficiency and low emissions for applications ranging from transportation to stationary power generation. At the heart of their functionality lies the catalyst layer (CL), a complex and heterogeneous structure responsible for facilitating key electrochemical reactions. The CL comprises multiple components, including catalyst nanoparticles, ionomers, and carbon black (CB), each contributing to the overall performance of the CL and cell.[1] Despite their importance, the formation and behavior of CLs remain poorly understood, with their random and multiscale structure, spanning from a few nanometers to micrometers, posing significant challenges for visualization and characterization. This issue has been highlighted by recent reviews, which note the lack of progress in understanding CL structure formation and its influence on PEM fuel cell performance, citing the limitations of existing techniques for probing such intricate systems.[2,3]

Among the CL components, CB plays a particularly critical role.[4] Several CB characteristics must be carefully controlled because of their relevance to CL performance, as highlighted in.[4] Most importantly, these include the surface area and pore size; CB electronic conductivity, which governs electron transport through the layer; and CB oxygen-containing functional groups, which control hydrophilicity and hydrophobicity and are therefore relevant to water management and platinum (Pt) functionalization. As a conductive support material for catalyst nanoparticles, CB directly impacts catalyst dispersion, stability, and activity. CB materials are composed of aggregates of spheroidal primary nanoparticles. These primary particles typically consist of an amorphous core surrounded by layers of polyaromatic carbon atoms arranged in a disordered, or "turbostratic," manner, forming nanosized domains.[5] This structure impacts electrical conductivity, which is also influenced by particle size and aggregation. Recrystallizing spherical CB particles at 2500−3000 °C can result in partially crystallized features with well-ordered domains but also in reduced porosity. The pore size distribution can influence the

Received: September 11, 2025
Revised: January 16, 2026
Accepted: January 22, 2026

transport of reactants and products within the CL.[6] Additionally, CB properties can be tailored to improve water management through the introduction of oxygen-containing functional groups, facilitating optimal hydration and minimizing flooding during operation.[4,7] Functional groups on the carbon surface can also be designed to facilitate more effective interactions between the electrocatalyst and ionomer, reducing the need for high catalysts loadings.[7] Nitrogen surface functionalities can help to guide Pt nanoparticle deposition as well as enhance the uniformity of the ionomer.[8] However, in order to fully realize the opportunities that such advanced CB design potentially offers, advanced experimental characterization techniques are needed.[8]

Despite the critical importance of CB and the CL, traditional characterization techniques include Raman spectroscopy to highlight defects in carbon and X-ray photoelectron spectroscopy (XPS)[2] to probe the presence of functional groups. Raman spectroscopy, while effective for identifying graphitic and disordered carbon phases, struggles to provide sufficient depth resolution, limiting its surface sensitivity and ability to distinguish nanoscale changes in chemical bonding. Similarly, XPS provides valuable surface chemical information, but its relatively poor lateral resolution, as illustrated in Figure 1,

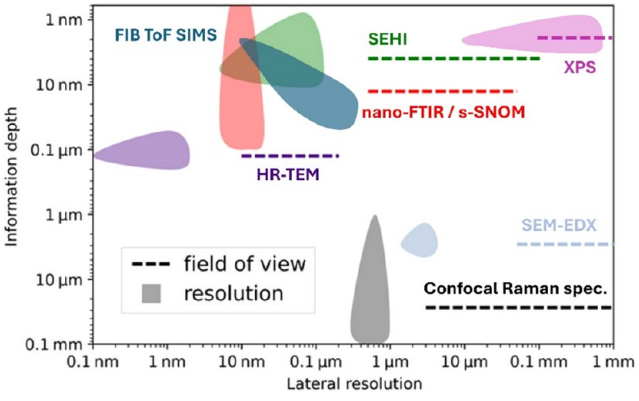

Figure 1. Plot of characterization techniques information reproduced and adapted with permission from Wiley[9] (John Wiley & Sons), © 2025. Additional information for XPS and FIB ToF SIMS was added. SEHI, confocal Raman spectroscopy, X-ray photoelectron spectroscopy (XPS), nano-Fourier transformed infrared spectroscopy (FTIR)/scattering scanning nearfield optical microscopy (s-SNOM), SEM -energydispersive X-ray analysis (EDX), and high-resolution transmission electron microscopy (HR-TEM). The shaded regions represent the resolution ranges with the dashed horizontal line showing the range of the horizontal field of view.

prevents the identification of localized chemical variations.[9] More recent approaches, including Focused Ion Beam combined with Time of Flight Secondary Ion Mass Spectrometry (FIB ToF SIMS) offers complementary chemical and molecular information, and when operated at low keV can achieve improved depth resolution. However, these methods are destructive, via ion beam damage or limited lateral resolution may restrict their ability to resolve nanoscale chemical environments within the CL. In parallel, fluorescence spectroscopy has also been integrated into FIB systems and can provide highly sensitive elemental detection, although it does not allow isotopic differentiation.[10] To address the challenges presented in the techniques above, Secondary Electron Hyperspectral Imaging (SEHI), based within a FIB-SEM could provide a solution.

SEHI is a type of low voltage SEM (LV-SEM) and hyperspectral imaging technique which leverages the energy selective collection of secondary electrons (SE) across a range of energies using a mirror electrode within the SEM. This approach generates hyperspectral data sets composed of sequentially collected high-resolution images, each corresponding to a specific energy range. SE spectra can then be derived from the stack for each pixel. Alternatively, image tiles (i.e 3 × 3 pixel square) might be used, where each tile has an associated SE spectrum. Where conventional SEM records only the total secondary electron yield, SEHI resolves the energy spectrum of the tiles.[11] Within the spectrum, peak positions can correspond to bonding states of specific elements. In this work, only peak position is used, as peak widths and heights are highly sensitive to experimental conditions and can vary significantly between instruments.[9] Based on peak position, SEHI can provide local surface chemistry and detailed compositional information down to the nanometer-scale[9,11,12] SEHI can be considered a technique which integrates the benefits of the high resolution imaging of LV-SEM with the surface sensitivity comparable to XPS. Its successful application across a range of materials systems, including polymers, biomaterials, and metallic surfaces, highlights its versatility and potential for advancing understanding in diverse applications.[9,11−18] For instance, it has been used for metal nanoparticle mapping in films aerosol jet printed from palladium−silver metal organic decomposition (MOD) inks[16] for the characterization of mechanochemically functionalized carbon black materials.[9,18]

Here, SEHI is applied to analyze key components of PEM fuel cells, with a focus on CB and ionomer films within the CL. By capturing secondary electron spectra and hyperspectral maps, we reveal the chemical and structural properties of different CB types and the interactions between ionomer membranes and their reinforcements. This work not only advances the characterization of PEM fuel cell materials but also establishes SEHI as a powerful tool for tackling longstanding challenges in the field.

2. MATERIALS AND METHODS

2.1. Materials

The study utilized four commercially available materials: two carbon black (CB) powders (graphitised and high-surface-area), a reinforced membrane, an ionomer solution, and a membrane with a catalyst layer comprising CB, Pt, and ionomer.

2.2. Cryo-Low Voltage (LV)-Scanning Electron Microscopy Imaging

Cryo-scanning electron microscopy (Cryo-SEM) was performed using the Quorum PP3010T Cryo-SEM preparation system (Quorum Technologies Ltd., Laughton, East Sussex, UK). For the carbon black (CB) powders, the materials were cryo-frozen onto a gold SEM shuttle with a thin layer of optimal cutting temperature compound (OCT) applied to the stub beforehand to aid adhesion. The sample for the reinforced membrane was freeze-fractured. The ionomer solution was cryo-frozen before imaging by pipetting the solution onto a specialized cryo-SEM stub, which was then plunge-frozen in liquid nitrogen slush. For the catalyst layer, comprising CB, Pt, and ionomer, a cryo-microtome cross-section was also prepared. Following sample preparation, the specimens were transferred to a cooled prep stage (−160 °C) and subsequently loaded onto the cryo-stage (−160 °C) within the SEM chamber for imaging. The full cryogenic conditions were used alongside an anticontaminator which was maintained in the

https://doi.org/10.1021/acsomega.5c09325
ACS Omega XXXX, XXX, XXX−XXX

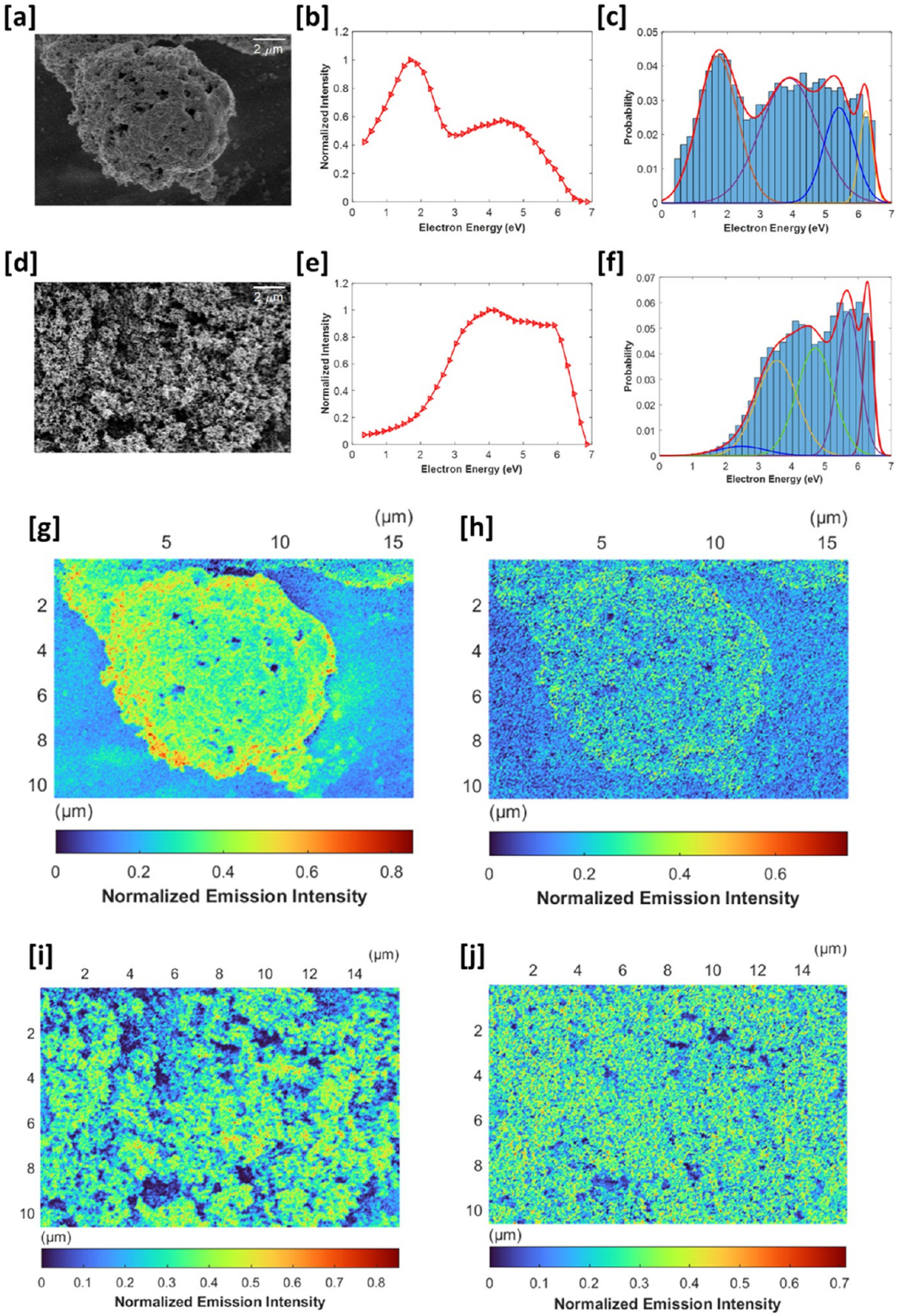

Figure 2. Secondary Electron Hyperspectral Imaging (SEHI) analysis of graphitised and high-surface-area (HSA) carbon blacks (CB). (a) SE image of graphitised CB. (b) Full field-of-view SE spectrum. (c) Decomposed SE spectra for graphitised CB showing peaks at 1.71 eV (graphitised carbon), 3.89 eV (amorphous carbon), and 5.41 eV (oxygen functionalities). Peaks above 6 eV are excluded to avoid topological artifacts. (d) SE image of HSA CB. (e) Full field-of-view SE spectrum. (f) Decomposed SE spectra for HSA CB showing peaks at 2.48 eV (amorphous carbon/sp2-carbon), 3.54 eV (amorphous carbon), 4.70 eV (hydroxyl groups), and 5.72 eV (CO bonding). (g) SEHI map of graphitised CB highlighting the spatial distribution of graphitised carbon (1.71 eV). (h) SEHI map of oxygen functionalities (Likely C−O) (5.41 eV) on graphitised CB. (i) SEHI map of amorphous carbon/sp2-carbon (2.48 eV) on HSA CB. (j) SEHI map of CO bonding (5.72 eV) on HSA CB. Maps reveal spatial variations in functional group distributions across CB surfaces.

https://doi.org/10.1021/acsomega.5c09325
ACS Omega XXXX, XXX, XXX−XXX

chamber at −185 °C to prevent buildup of contamination and sample damage when obtaining sequential SEHI measurements.

Observation of the surface morphology of all materials was performed using a Duelbeam FIB-SEM (Helios Nanolab G3). Samples were not subject to the additional deposition of a conductive coating. A low accelerating voltage (1 kV) with a typical vacuum pressure of 10^{-7} mbar at a working distance of 4 mm was applied. An Everhart-Thornley Detector (ETD) for low magnification and a Through Lens Detector (TLD) for high magnification were used for the collection of SE images.

2.3. Secondary Electron Hyperspectral Imaging (SEHI)

The process of SEHI data acquisition has been described in detail in previous studies.[9,12] Briefly, SEHI generation in this study was performed using the Helios Nanolab G3 microscope by applying consistent operating conditions of 1 keV and 50 pA primary electron beam and imaging in immersion mode by the TLD. To ensure that images were taken of the true CL surface, no conductive coating was applied to the samples in contrast to typical SEM analysis practice. At the time of analysis, a typical vacuum pressure of $\sim 10^{-7}$ mbar was maintained at a working distance of 4 mm. The collection of SEHI of different energy ranges was enabled through the adjustment of the mirror electrode voltage (MV) together with a tube bias setting of 150 V. Stepping the MV in a range of −15 to 15 V was achieved using an automatic iFast collection recipe.[19]

3. RESULTS AND DISCUSSION

The results and discussion in this study are structured to analyze the key components within PEM fuel cells, focusing on their individual properties and interactions. First, the analysis centers on carbon black (CB), examining two types with distinct characteristics: graphitised CB and high-surface-area CB in section 3.1. This allows us to elucidate the chemical features and bonding environments that underpin their roles as catalyst supports. Next, we explore the reinforcement membrane, specifically the PBI layer in section 3.2. Finally, we examine a complete membrane assembly that includes a catalyst layer comprising CB, Pt nanoparticles, and ionomer, representing the full functional structure of the CL (3.3).

3.1. Chemical and Structural Characterization of Carbon Black

Figure 2 highlights the SEHI analysis of two types of carbon black (CB): graphitised CB (Figure 2a−c,g,h) and high-surface-area (HSA) CB (Figure 2d−f,i,j). Panel (Figure 2a) displays a low voltage, secondary electron (SE) image of the graphitised CB, while panel (Figure 2b) presents the full field-of-view SE spectrum. Following component analysis,[11] the decomposed SE spectra in panel (Figure 2c) reveal four peak positions of 1.71, 3.89, 5.41, and 6.22 eV. Peaks above 6 eV should be excluded from SEHI analysis to minimize artifacts due to surface topography.[9,18] Based on prior literature and experimental findings,[9,11,13,20,21] the 1.71 eV peak corresponds to graphitised carbon, 3.89 eV to amorphous carbon, and 5.41 eV to oxygen-containing functionalities (likely C−O [Based on Figure 16 ref 9]). Panels (Figure 2g) and (Figure 2h) show SEHI maps corresponding to the spatial distribution of graphitised regions (1.71 eV) and oxygen functionalities (5.41 eV) on the graphitised CB surface.

Similarly, panels (Figure 2d−f) depict the SE image and spectra for HSA CB. The decomposed spectra in panel (Figure 2f) include five peaks at 2.48, 3.54, 4.70, 5.72, and 6.31 eV. The peaks are assigned to amorphous carbon/sp2-carbon[9,11,20,21] (2.48 eV), amorphous carbon (3.54 eV), hydroxyl groups (4.70 eV), and CO bonding (5.72 eV), with the 6.31 eV peak excluded for consistency. Panels (Figure 2i,j) illustrate SEHI maps of amorphous carbon (2.48 eV) and CO bonding (5.72 eV) for the HSA CB. Across all maps, functional groups exhibit distinct spatial distributions, with variations in intensity highlighting heterogeneity on the CB surfaces. Notably, no evidence for charging artifacts was observed within this data set, data sets exhibiting charging artifacts were excluded from analysis.

For the graphitised CB, visualizing graphitised carbon regions is crucial for understanding the structural and electrochemical properties of materials used in fuel cells. As shown in panel (Figure 2g), graphitised carbon exhibits a well-ordered structure, which significantly enhances electrical conductivity. SEHI also provides the Gaussian mixing proportion for each fitted SE component, indicating the relative contribution of SEs emitted at each characteristic energy.[11] These proportions do not represent the material's chemical composition, but instead reflect the relative intensity of SE emission from different environments. As shown in Table 1 for graphitised CB, the ω component associated with graphitic bonding (1.71 eV), has a high contribution. Indicating a strong presence of graphitic carbon. This value could be used to compare samples in an effort to improve the overall graphitic carbon contribution provided identical imaging conditions and instruments are used. This characteristic is essential for fuel cell performance, as efficient electron transport is necessary for the catalyst's effectiveness and the overall efficiency of the cell. The high conductivity of graphitised carbon not only supports better electron flow but also contributes to the durability of the catalyst support by minimizing the risk of local resistance. This ensures stable power output over time, improving the longevity and reliability of the fuel cell.

Table 1. GMM Clustering Results for Graphitised CB[a]

	Gaussian components			
model parameter	GMM1	GMM2	GMM3	GMM4
ω (%)	33.79	41.75	17.20	7.26
μ (eV)	**1.71**	**3.89**	**5.41**	**6.22**
σ (eV)	0.60	0.87	0.47	0.21

[a]**ω**: Component mixing proportion, **μ**: Mean peak value, **σ**: Peak uncertainty value.

In the case of HSA CB, the visualization of amorphous carbon/sp2-carbon (2.48 eV) and CO bonding (5.72 eV) in SEHI maps provides valuable insights into material properties that impact fuel cell development. The absence of a clear graphitic peak in HSA CB, as shown in panel (Figure 2e), would indicate a lower graphitic carbon content, thus is likely to reduce the materials conductivity. Moreover, these amorphous carbon regions, which are typically less conductive than graphitic carbon, can create areas of resistance within the carbon support material. Mapping these regions helps assess the uniformity of the carbon structure, which is critical for ensuring consistent catalyst performance.[22]

Additionally, the distribution of CO bonding, indicative of surface oxidation or functionalization, plays an important role in the interaction between the catalyst and the carbon support.[22] The more prominent peaks corresponding to hydroxyl and oxygen containing functional groups present in HSA CB (4.7 and 5.7 eV) indicate a much higher level of surface oxidation which can be beneficial for both catalyst dispersion and wettability. These characteristics would result in an overall improvement in catalyst performance. However, excessive functionalization can lead to a reduction in conductivity and potentially compromise the structural integrity of the support.

https://doi.org/10.1021/acsomega.5c09325
ACS Omega XXXX, XXX, XXX−XXX

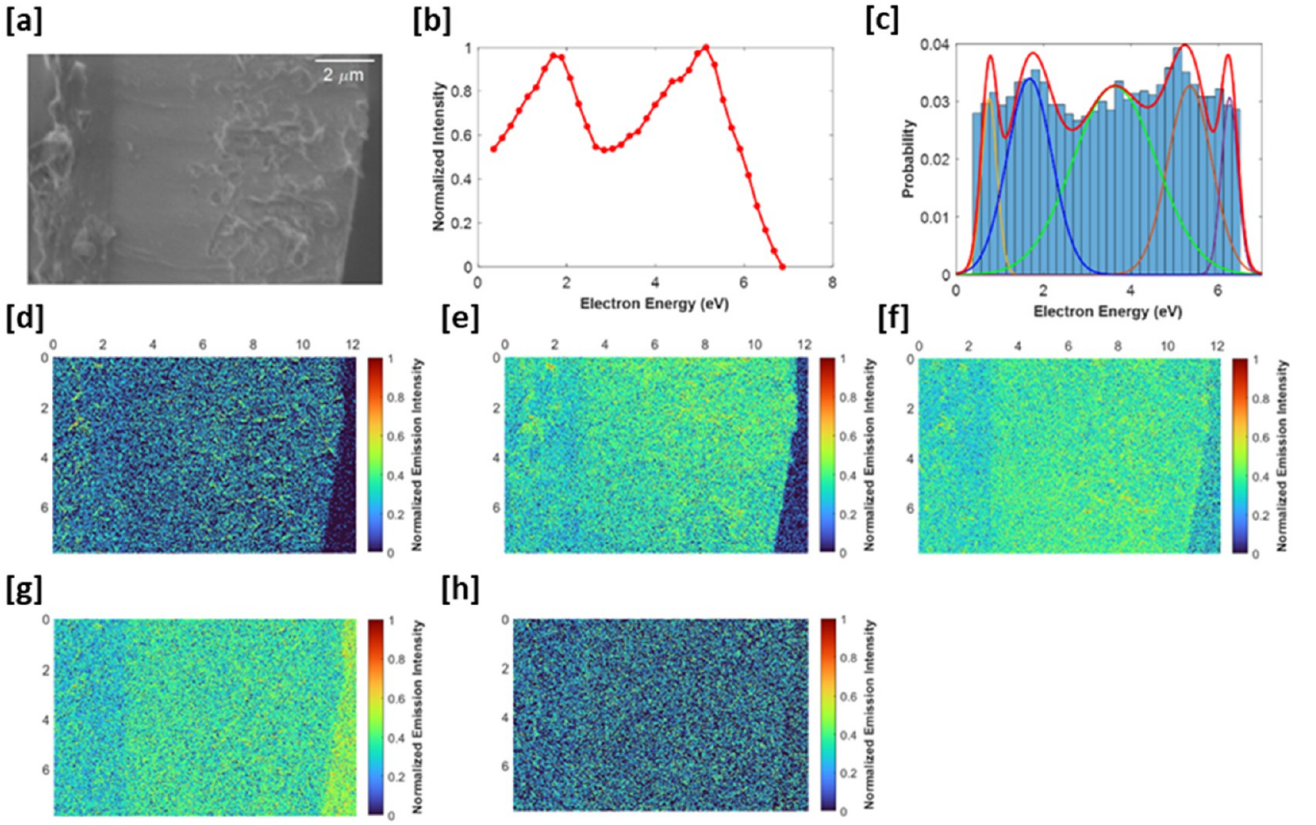

Figure 3. SEHI analysis of a cross-sectioned membrane supported by a reinforcement. (a) SE image showing the reinforcement (left), membrane (center), and SEM carbon tab (right). (b) Full field-of-view SE spectrum. (c) Decomposed spectra with peaks at 0.76 eV (C1), 1.68 eV (C2, amorphous carbon), 3.63 eV (C3, sp2 bonding), 5.35 eV (C4, oxygen functionalities), and 6.26 eV (C5). (d–h) SEHI maps for C1–5, highlighting the spatial distribution of chemical functionalities.

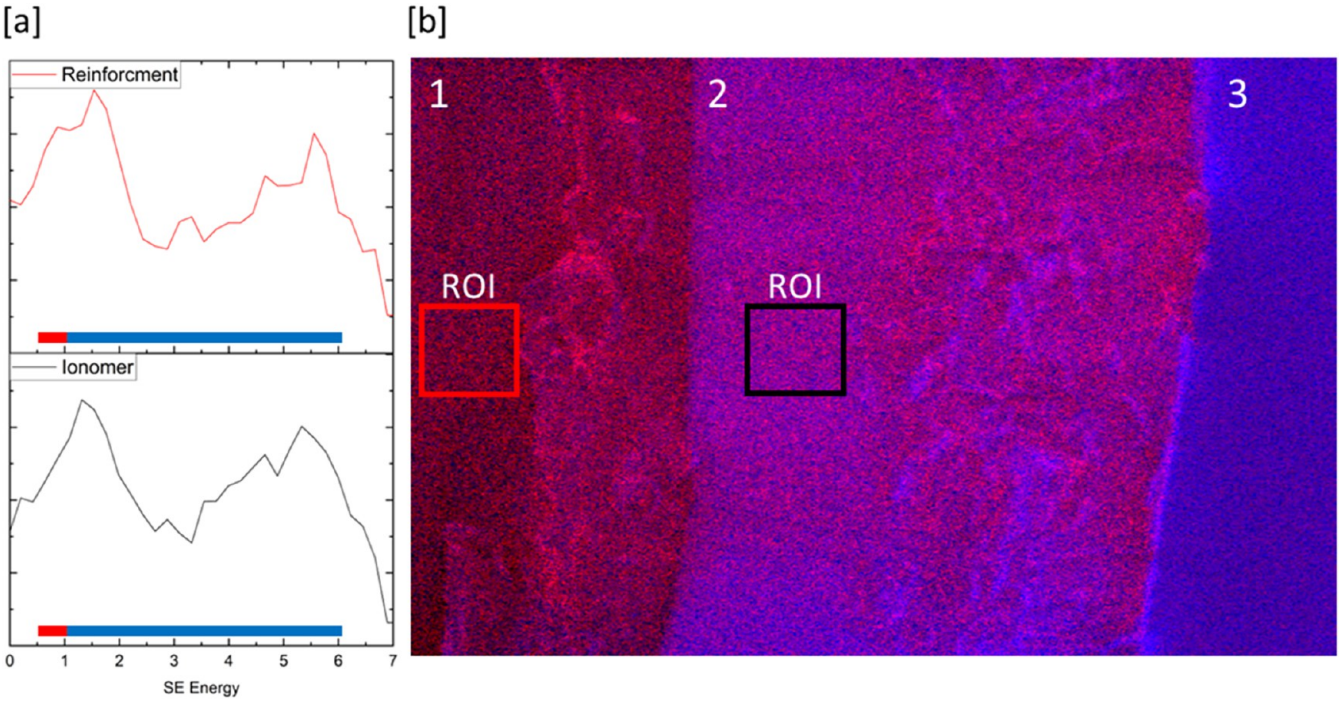

Figure 4. SEHI analysis of a cross-sectioned membrane supported by a reinforcement. (a) SE spectra from a 1 μm^2 region of interest (ROI) within the reinforcement and the membrane; a distinct peak at 0.8 eV is unique to the reinforcement. (b) RGB SEHI map (15 μm HWF) using red (0.5–1 eV) to represent the reinforcement-associated 0.8 eV peak and blue (1–6 eV) for other emissions; red regions confirm localization of the 0.8 eV peak within the reinforcement, attributed to nitrogen bonding. Labels: (1) reinforcement, (2) membrane, (3) carbon tab.

https://doi.org/10.1021/acsomega.5c09325
ACS Omega XXXX, XXX, XXX−XXX

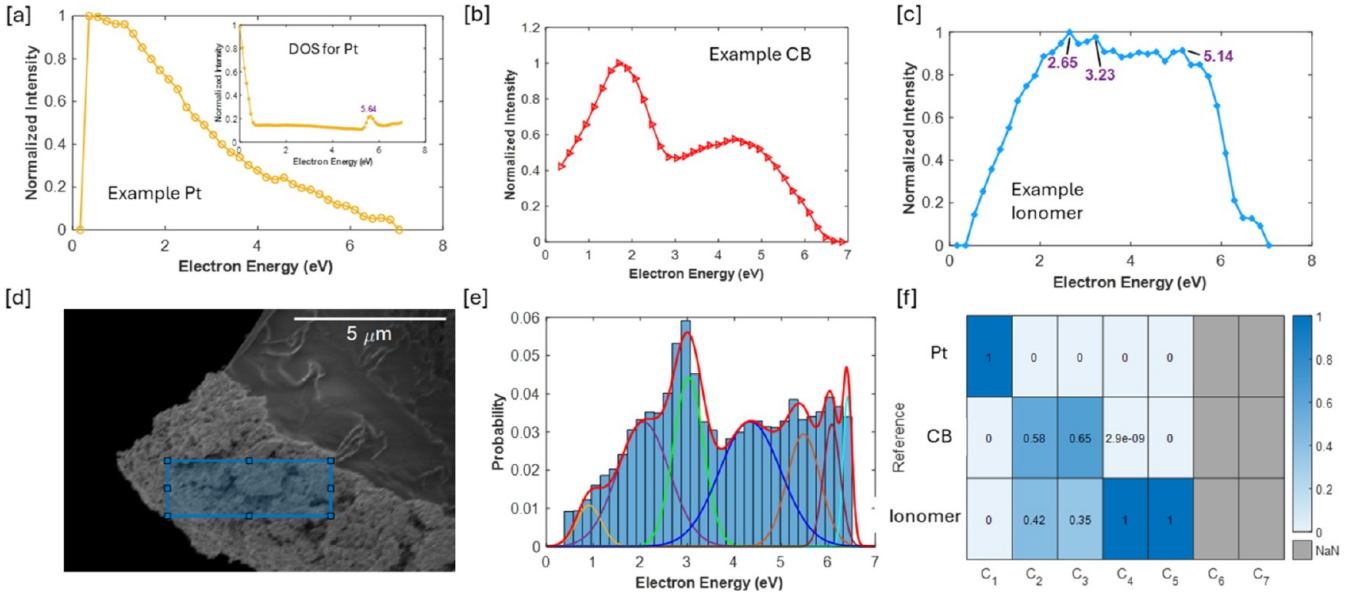

Figure 5. Panels (a−c) show reference data sets for platinum (Pt), carbon black (CB), and ionomer, respectively. (a) SE spectrum of Pt deposited using FIB, with an inset showing the theoretical density of states (DOS) of Pt, revealing peaks at 0.2 and 5.6 eV that correspond to the observed Pt spectrum. DOS data derived from Materials Project (https://doi.org/10.17188/1189002). (b) SE spectrum for CB, with specific peaks of interest highlighted. (c) SE spectrum for the ionomer, showing characteristic peaks. Panels (d−f) focus on the SEHI analysis of the CL data set. (d) SE image of the region of interest (ROI) analyzed. (e) SE spectrum for the CL, showing seven components: C1 (0.91 eV), C2 (2.07 eV), C3 (3.03 eV), C4 (4.34 eV), C5 (5.47 eV), C6 (6.07 eV), and C7 (6.41 eV). (f) Probability map showing the assignment of components to Pt (C1), ionomer (C4 and C5), and CB (C3). C6 and C7 are excluded from further analysis as they are above 6 eV.

Carbon oxidation/corrosion is one of the main concerns for the long-term stability of cell assembly and the carbon corrosion process is not well understood due to its complexity and difficulties in tracing the evolution of carbon corrosion. Thus, the ability of mapping CO bonding sites is a useful tool for investigating the carbon corrosion process.

In the case of CB SEHI has revealed a clear trade-off between the samples, where graphitised CB offers better conductivity and stability, HSA CB provides an enhanced surface functionality suited to better catalyst dispersion and wettability.

3.2. Analysis of the PBI Reinforcement Membrane

Figure 3 illustrates the SEHI analysis of a cross-section of a membrane supported by a reinforcement. Panel (Figure 3a) shows an SE image of the sample, with the reinforcement on the left, the membrane in the middle, and the SEM carbon tab on the right. Panel (Figure 3b) presents the full-field SE spectrum, while panel (Figure 3c) shows the decomposed spectra after component analysis. The analysis identifies five components (C) analysis defined peaks: 0.76 eV (C1), 1.68 eV (C2), 3.63 eV (C3), 5.35 eV (C4), and 6.26 eV (C5). SEHI maps corresponding to these components are shown in panels (Figure 3d−h), revealing key insights into the material's chemical distribution. C2 highlights variations in sp2-carbon, C3 reveals strong a-CH bonding concentrated in the membrane, and C4 indicates oxygen-containing functionalities (likely C−O), also prominent in the membrane but diminished in the reinforcement.

To address limitations of the full-field spectra in detecting subtle spectral features, smaller regions of interest (ROIs) of 1 μm^2 were selected within the reinforcement and membrane. The resulting spectra, shown in Figure 4a for the reinforcement and membrane, respectively, reveal distinguishing features. A peak at 0.8 eV is prominent in the reinforcement but absent in the membrane, while several peaks between 4−5 eV are significant in the membrane but not in the reinforcement. Based on previous studies[23] this feature is likely associated with nitrogen bonding within the reinforcement, distinguishing it from the membrane. To further differentiate the materials, an RGB-based SEHI color mapping technique was applied,[12] with red (0.5−1 eV) capturing the 0.8 eV emission peak and blue (1−6 eV) representing other emissions. The RGB image shown in Figure 4b clearly shows predominately red-colored regions localized within the reinforcement, confirming its unique SE peaks.

Identifying the reinforcement is crucial for understanding its role in fuel cell systems. Reinforcements are commonly used in high-temperature PEMFCs because of their excellent thermal and chemical stability, as well as their proton conductivity at elevated temperatures. However, their performance can be affected by the distribution of functional groups within the reinforcement, which can influence both proton transport and the membrane's interaction with other materials in the fuel cell. The identification of specific peaks, such as the 0.8 eV emission associated with nitrogen bonding in the reinforcement, helps distinguish it from other components, such as the membrane or carbon supports. Understanding the spatial distribution of nitrogen-containing functional groups within the reinforcement is important for optimizing its ionic conductivity and stability. Moreover, by detecting specific peaks related to the reinforcement, it is possible to map areas where structural or compositional changes may occur, aiding in the development of more durable and efficient fuel cell membranes. The identification of these regions also enables better differentiation between the reinforcement and other components, such as the membrane and carbon substrates. This ensures a more accurate analysis of fuel cell materials and their interactions, helping to optimize fuel cell design and performance for long-term applications.

https://doi.org/10.1021/acsomega.5c09325
ACS Omega XXXX, XXX, XXX−XXX

3.3. Analysis of the Catalyst Layer

The analysis of the CL within the membrane assembly is conducted using SEHI data, which is essential for identifying and mapping the distribution of materials such as Pt, CB, and ionomer. To facilitate this analysis, reference data sets for Pt, CB, and ionomer are first established (Figure 5, panels a−c).

Panel (Figure 5a) shows an example SE spectrum collected from Pt, which was deposited using focused ion beam-induced deposition via a gas injection system (GIS) with a Pt-organometallic precursor. Although the Pt deposition is not 100% pure and contains some carbon contamination, we verified that this contamination does not significantly affect the spectral analysis. The inset in panel (Figure 5a) displays the theoretical density of states (DOS) for Pt, which shows two characteristic peaks: one around 0.2 eV and another at approximately 5.6 eV. The 0.2 eV peak, together with the overall spectral shape, aligns closely with that of the SE spectrum of the Pt sample, confirming that this data set is suitable for use as a reference for subsequent analysis. Panels (Figure 5b) and (Figure 5c) provide similar reference data for CB and ionomer, respectively, highlighting specific peaks that will be used to identify these materials in the catalyst layer data.

The analysis of the catalyst layer itself is presented in panels (Figure 5d−f). Panel (Figure 5d) displays the SE image of the ROI selected for SEHI analysis. Panel (Figure 5e) shows the corresponding SE spectrum for the CL, with seven components identified at the following energies: C1 (0.91 eV), C2 (2.07 eV), C3 (3.03 eV), C4 (4.34 eV), C5 (5.47 eV), C6 (6.07 eV), and C7 (6.41 eV). As we do not consider peaks above 6 eV, C6 and C7 are excluded from further analysis. With these components identified, we can proceed to assign them to the reference materials using a probability map (Figure 5f). The probability map clearly indicates that C1 strongly corresponds to Pt, C4 and C5 are most likely associated with the ionomer, and C3 has a 65% probability of being linked to CB, making it the most likely candidate for identifying carbon in the CL layer.

Following this, Figure 6 presents the SEHI maps linked to the identified components. Panel (Figure 6a) shows the SEHI map for Pt, panel (Figure 6b) for CB, and panel (Figure 6c) for the ionomer. These maps reveal the spatial distributions of each material within the CL, providing insights into the composition and heterogeneity of the layer. It is important to note that the ability to visualize the variations of these components within the CL is crucial for understanding the structural integrity and performance of the catalyst. By mapping the spatial distributions, we can assess how each material contributes to the overall functionality of the fuel cell, particularly in relation to catalyst support, ion transport, and overall efficiency.

Figure 7 offers a comparative analysis between the spatial distributions of CB and ionomer in the same region. This panel presents a magnified view of smaller regions within the CL, revealing that areas with high CB content show little ionomer content, while regions surrounding the CB display higher ionomer intensity. This suggests that the ionomer and CB are in close spatial proximity, indicating potential interactions between them. These interactions are likely governed by van der Waals and electrostatic forces, which are known to depend on the surface functionalities of the specific carbon black used.[24] Such interactions may contribute to the structural stabilization of the catalyst layer. The horizontal field of view for this panel is 100 nm, providing context for the level of resolution at which these distributions are visualized. This level of detail is not only unique to SEHI but crucial for understanding the interplay between materials and their collective role in enhancing fuel cell performance.

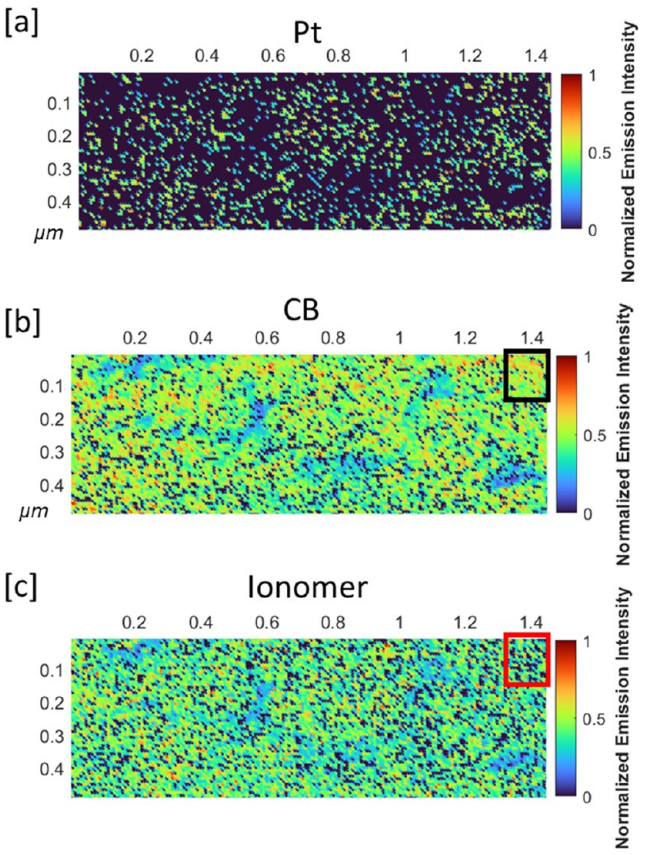

Figure 6. Panels (a−c) show the SEHI maps of Pt, CB, and ionomer, respectively, with each map corresponding to components identified in Figure 5. These maps highlight the spatial distribution of each material within the CL. (a) Pt map, (b) CB map, and (c) ionomer map.

3.4. Future Perspectives

SEHI holds significant promise for advancing the understanding of PEMFCs, especially in the context of optimizing the chemical composition and structure of the catalyst layers, ionomer films, and reinforced membranes. Future research should focus on expanding the application of SEHI to other materials commonly used in PEMFCs, such as various alternative catalyst supports, to further investigate their structural properties and their interaction with the surrounding media. Further work is also needed to enhance the data analysis capabilities of SEHI, particularly in handling complex spectra and improving the quantification of specific chemical species. This will require the development of more sophisticated algorithms for spectral decomposition and mapping, which could aid in the more precise identification of minor chemical components and subtle variations in surface functionalization. Moreover, the scalability of SEHI in high-throughput analysis should be explored, as it has the potential to streamline the characterization process for large numbers of samples, which is crucial for the development of industrial-scale PEMFC technologies. Ultimately, continued advancements in SEHI technology, coupled with a deeper understanding of material behavior at the nanoscale, will drive the development of more efficient, durable, and cost-effective PEMFCs for a range of sustainable energy applications.

https://doi.org/10.1021/acsomega.5c09325
ACS Omega XXXX, XXX, XXX−XXX

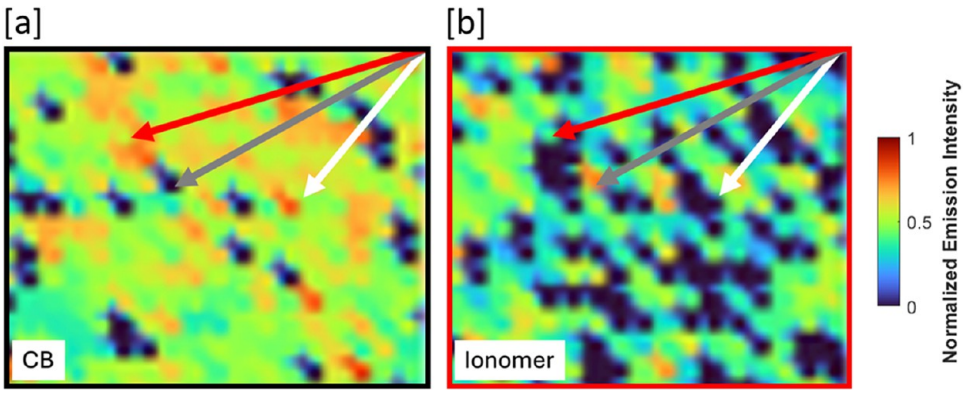

Figure 7. Comparative SEHI analysis of CB (a) and ionomer (b) in the same region (as marked in Figure 6). The magnified views show that areas of high CB intensity (white arrow) exhibit minimal ionomer content, while regions of low intensity CB show higher ionomer intensity (gray arrow) the red arrow highlights a region in which both CB and ionomer coexist.

4. CONCLUSION

This study explored the potential of SEHI in the analysis of PEM fuel cell components, focusing on CB and ionomer films. SEHI, integrated within a FIB–SEM, provided chemical sensitivity, spatial resolution, and surface specificity, revealing detailed insights into the chemical and structural properties of these materials at the nanoscale. Through the analysis of graphitised and high-surface-area CB, SEHI identified critical structural features that influence catalyst stability and electron transport. Additionally, SEHI successfully mapped the interaction between the ionomer membranes and their PBI reinforcement, distinguishing key chemical differences. These findings highlight the value of SEHI as a powerful tool for characterizing the complex and heterogeneous components of PEM fuel cells, offering new perspectives on material optimization for improved fuel cell performance and durability.

■ ASSOCIATED CONTENT

Supporting Information

The Supporting Information is available free of charge at https://pubs.acs.org/doi/10.1021/acsomega.5c09325.

SEHI map of amorphous carbon (3.89 eV) on the graphitised CB sample and an SEHI map reproduced from the manuscript of graphitic carbon (1.71 eV) (PDF)

■ AUTHOR INFORMATION

Corresponding Author

Nicholas T. H. Farr − *School of Chemical, Materials and Biological Engineering, University of Sheffield, Sheffield S1 3JD, U.K.*; orcid.org/0000-0001-6761-3600; Email: n.t.farr@Sheffield.ac.uk

Authors

Martha Briceno de Gutierrez − *Johnson Matthey Technology Centre, Sonning Common RG4 9NH, U.K.*

Mark S'ari − *Johnson Matthey Technology Centre, Sonning Common RG4 9NH, U.K.*

Ben Garton − *School of Chemical, Materials and Biological Engineering, University of Sheffield, Sheffield S1 3JD, U.K.*

Jingqiong Zhang − *School of Electrical and Electronic Engineering, The University of Sheffield, Sheffield S1 3JD, U.K.*

Lyudmila S. Mihaylova − *School of Electrical and Electronic Engineering, The University of Sheffield, Sheffield S1 3JD, U.K.*; orcid.org/0000-0001-5856-2223

Cornelia Rodenburg − *School of Chemical, Materials and Biological Engineering, University of Sheffield, Sheffield S1 3JD, U.K.*

Complete contact information is available at: https://pubs.acs.org/10.1021/acsomega.5c09325

Notes

The authors declare no competing financial interest.

■ ACKNOWLEDGMENTS

N.T.H.F., J.Z., L.S.M., and C.R. acknowledge EPSRC for funding through SEE MORE MAKE MORE (EP/V012762/1). The authors also acknowledge the Sorby Centre for Electron Microscopy at the University of Sheffield for access to electron microscopy facilities and analytical support, and thank Dr. Jiahui Qi for the deposition of the Pt reference. We further thank Johnson Matthey for also part-funding the experimental work. For the purpose of open access, the authors have applied a Creative Commons Attribution (CC BY) licence to any Author Accepted Manuscript version arising.

■ REFERENCES

(1) Xie, Z.; Yu, S.; Yang, G.; Li, K.; Ding, L.; Wang, W.; Zhang, F.-Y. Optimization of Catalyst-Coated Membranes for Enhancing Performance in Proton Exchange Membrane Electrolyzer Cells. *Int. J. Hydrogen Energy* **2021**, *46*, 1.

(2) Zhao, J.; Liu, H.; Li, X. Structure, Property, and Performance of Catalyst Layers in Proton Exchange Membrane Fuel Cells. *Electrochem. Energy Rev.* **2023**, *6*, No. 13.

(3) Schlüter, N.; Novák, P.; Schröder, D. Nonlinear Electrochemical Analysis: Worth the Effort to Reveal New Insights into Energy Materials. *Adv. Energy Mater.* **2022**, *12*, No. 2200708.

(4) Amin, A. S.; Caidi, A.; Lange, T.; Radev, I.; Sandbeck, D. J. S.; Philippi, W.; Kräenbring, M.-A.; Öztürk, M.; Peinecke, V.; Lerche, D.; Özcan, F.; Segets, D. Key Control Characteristics of Carbon Black Materials for Fuel Cells and Batteries for a Standardized Characterization of Surface Properties. *Part. Part. Syst. Charact.* **2025**, *42*, No. 2400069.

(5) Isagoda, M.; Ariyoshi, Y.; Fujita, Y.; et al. Unveiling the Surface of Carbon Black via Scanning Probe Microscopy and Chemical State Analysis. *Carbon Trends* **2024**, *16*, No. 100378.

(6) Park, J.; Kwon, O.; Oh, H.-M.; Jeong, S.; So, Y.; Park, G.; Jang, H.; Yang, S.; Baek, J.; Kim, G.; Park, T. Optimizing Design of Catalyst Layer Structure with Carbon-Supported Platinum Weight Ratio Mixing Method for Proton Exchange Membrane Fuel Cells. *Energy* **2024**, *291*, No. 130363.

(7) Kumar, A.; Park, E. J.; Kim, Y. S.; Spendelow, J. S. Surface Functionalization of Carbon Black for PEM Fuel Cells. *Macromol. Chem. Phys.* **2024**, *225*, No. 2400092.
(8) Horst, R. J.; Forner-Cuenca, A. Electrode Engineering Strategies to Advance Polymer Electrolyte Fuel Cells. *Curr. Opin. Chem. Eng.* **2024**, *46*, No. 101053.
(9) Nohl, J. F.; Farr, N. T.; Acocella, M. R.; Knight, A. J.; Hughes, G. M.; Zhang, J.; Robertson, S.; Micklethwaite, S.; Murphy, S.; Motlová, T.; Walker, C.; Tartakovskii, A. I.; Mika, F.; Pokorná, Z.; Tear, S.; Pratt, A.; Ford, N. L.; Hondow, N.; Jepson, M. A. E.; Mihaylova, L. S.; Reeves-McLaren, N.; Cussen, S. A.; Rodenburg, C. Secondary Electron Hyperspectral Imaging of Carbons: New Insights and Good Practice Guide. *Adv. Sci.* **2025**, *12*, No. e01907.
(10) Budnik, G.; Scott, J. A.; Jiao, C.; Maazouz, M.; Gledhill, G.; Fu, L.; Tan, H. H.; Toth, M. Nanoscale 3D Tomography by In-Flight Fluorescence Spectroscopy of Atoms Sputtered by a Focused Ion Beam. *Nano Lett.* **2022**, *22* (20), 8287.
(11) Zhang, J.; Farr, N. T. H.; Nohl, J.; et al. Toward Automated Chemical Analysis of Materials Using Secondary Electron Hyperspectral Imaging and Unsupervised Learning. *IEEE Access* **2025**, *13*, 173976−174000.
(12) Nohl, J. F.; Farr, N. T. H.; Sun, Y.; Hughes, G. M.; Stehling, N.; Zhang, J.; Longman, F.; Ives, G.; Pokorná, Z.; Mika, F.; Kumar, V.; Mihaylova, L.; Holland, C.; Cussen, S. A.; Rodenburg, C. Insights into Surface Chemistry Down to Nanoscale: An Accessible Colour Hyperspectral Imaging Approach for Scanning Electron Microscopy. *Mater. Today Adv.* **2023**, *19*, No. 100413.
(13) Farr, N. T. H.; Roman, S.; Schäfer, J.; Quade, A.; Lester, D.; Hearnden, V.; MacNeil, S.; Rodenburg, C. A Novel Characterisation Approach to Reveal the Mechano−Chemical Effects of Oxidation and Dynamic Distension on Polypropylene Surgical Mesh. *RSC Adv.* **2021**, *11*, 34710−34723.
(14) Farr, N. T. H.; Hamad, S.; Gray, E.; Magazzeni, C.; Longman, F.; Armstrong, D.; Foreman, J.; Claeyssens, F.; Green, N.; Rodenburg, C. Identifying and Mapping Chemical Bonding within Phenolic Resin Using Secondary Electron Hyperspectral Imaging. *Polym. Chem.* **2021**, *12*, 177−182.
(15) Farr, N. T. H.; Pasniewski, M.; de Marco, A. Assessing the Quality of Oxygen Plasma Focused Ion Beam (O-PFIB) Etching on Polypropylene Surfaces Using Secondary Electron Hyperspectral Imaging. *Polymers* **2023**, *15*, 3247.
(16) Farr, N. T. H.; Davies, M.; Nohl, J.; Abrams, K. J.; Schäfer, J.; Lai, Y.; Gerling, T.; Stehling, N.; Mehta, D.; Zhang, J.; Mihaylova, L.; Willmott, J. R.; Black, K.; Rodenburg, C. Revealing the Morphology of Ink and Aerosol Jet Printed Palladium-Silver Alloys Fabricated from Metal Organic Decomposition Inks. *Adv. Sci.* **2024**, *11*, No. 2306561.
(17) Nohl, J.; Farr, N. T. H.; Acocella, M. R.et al. An Accessible Secondary Electron Hyperspectral Imaging Approach to Draw Meaningful Insights from Scanning Electron Microscopy. In *BIO Web Conf. 2024, 17th European Microscopy Congress (EMC 2024)*; EDP Sciences: Copenhagen, Denmark, Aug 25−30, 2024.
(18) Nohl, J. F.; Farr, N. T. H.; Sun, Y.; Hughes, G. M.; Cussen, S. A.; Rodenburg, C. Low-Voltage SEM of Air-Sensitive Powders: From Sample Preparation to Micro/Nano Analysis with Secondary Electron Hyperspectral Imaging. *Micron* **2022**, *156*, No. 103234.
(19) Stehling, N.; Jiao, C.; Abrams, K.; Rodenburg, C.Automatic iFAST Spectral Acquisition (Step 0.6 V Range−15−20.4 V); The University of Sheffield *Software* 2019, DOI: 10.15131/shef.data.7845044.v1.
(20) Farr, N.; Thanarak, J.; Schäfer, J.; Quade, A.; Claeyssens, F.; Green, N.; Rodenburg, C. Understanding Surface Modifications Induced via Argon Plasma Treatment through Secondary Electron Hyperspectral Imaging. *Adv. Sci.* **2021**, *8*, No. 4.
(21) Farr, N.; Pashneh-Tala, S.; Stehling, N.; Claeyssens, F.; Green, N.; Rodenburg, C. Characterizing Cross-Linking Within Polymeric Biomaterials in the SEM by Secondary Electron Hyperspectral Imaging. *Macromol. Rapid Commun.* **2020**, *41*, No. 3.
(22) Liu, F.; Gao, Z.; Su, J.; Guo, L. Understanding the Process of Carbon Corrosion and Its Impact on Performance Degradation during Simulated Start−Stop Operations for the Proton Exchange Membrane Fuel Cell. *Electrochim. Acta* **2023**, *468*, No. 143193.
(23) Elghazy, E.; Davies, M. M. J.; Farr, N. T. H.; Rodenburg, C.; Willmott, J. R.; Pandhal, J. Capturing Microalgae within Aerosols Provides Carbon Capture Bio-Functionality. *J. CO2 Util.* **2025**, *92*, No. 103024.
(24) Yang, F.; Xin, L.; Uzunoglu, A.; Qiu, Y.; Stanciu, L.; Ilavsky, J.; Li, W.; Xie, J. Investigation of the Interaction between Nafion Ionomer and Surface Functionalized Carbon Black Using Both Ultrasmall Angle X-ray Scattering and Cryo-TEM. *ACS Appl. Mater. Interfaces* **2017**, *9* (7), 6530.

https://doi.org/10.1021/acsomega.5c09325
ACS Omega XXXX, XXX, XXX−XXX